



Simulated and observed horizontal inhomogeneities of optical thickness of Arctic stratus

Michael Schäfer^{1,*}, Katharina Loewe^{2,*}, André Ehrlich¹, Corinna Hoose², and Manfred Wendisch¹

¹Leipzig Institute for Meteorology, University of Leipzig, Leipzig, Germany

²Institute of Meteorology and Climate Research, Karlsruhe Institute of Technology, Karlsruhe, Germany

*Both authors contributed equally to this work.

Correspondence: Michael Schäfer (michael.schaefer@uni-leipzig.de), Katharina Loewe (katharina.loewe@kit.edu)

Abstract. Two-dimensional (2D) horizontal fields of cloud optical thickness derived from airborne measurements of solar spectral radiance during the Vertical Distribution of Ice in Arctic Clouds (VERDI) campaign (carried out in Inuvik, Canada in April/May 2012) are compared with semi-idealized Large Eddy Simulations (LES) of Arctic stratus performed with the Consortium for Small-Scale Modeling (COSMO) atmospheric model. The input for the LES is obtained from collocated airborne dropsonde observations. Four consecutive days of a persistent Arctic stratus observed above the sea-ice free Beaufort Sea are selected for the comparison. Macrophysical cloud properties such as cloud top altitude and vertical extent are well captured by COSMO. Cloud horizontal inhomogeneity quantified by the standard deviation and one-dimensional (1D) inhomogeneity parameters show that COSMO produces only half of the measured horizontal cloud inhomogeneities, while the directional structure of the cloud inhomogeneity is well represented by the model. Differences between the individual cases are mainly associated with the wind shear near cloud top and the vertical structure of the atmospheric boundary layer. A sensitivity study changing the wind velocity in COSMO by a vertically constant scaling factor shows that the directional cloud inhomogeneity structures strongly depend on the mean wind speed. A threshold wind velocity is identified, which determines when the cloud inhomogeneity stops increasing with increasing wind velocity.

1 Introduction

Arctic clouds are expected to be a major contributor to the so-called Arctic Amplification (Serreze and Barry, 2011; Wendisch et al., 2017) and, therefore, need to be represented adequately in model projections of the future Arctic climate (Vavrus, 2004). Especially, low-level Arctic stratus are of importance (Wendisch et al., 2013), because they occur quite frequently (around 40%, Shupe et al., 2006, 2011), typically persist over several days or even weeks (Shupe et al., 2011), and on annual average, warm the Arctic surface (Shupe and Intrieri, 2004). The numerous physical and microphysical processes that determine the properties of Arctic stratus are complexly linked to each other (e.g., Curry et al., 1996) and still not understood in full detail (Morrison et al., 2012). Some are explained in the following: Arctic stratus often appears in mixed phase state (liquid water and solid ice coexist, McFarquhar et al., 2007; Mioche et al., 2015) and, therefore, the cloud should glaciate rapidly due to the Wegener-Bergeron-Findeisen process. However, this is not the case. A mixed-phase Arctic stratus can still persist for several days or even weeks. Dynamic factors (updrafts), which increase the actual supersaturation in the cloud beyond the equilibrium



values for both liquid water and ice, and a steady supply of water vapor from above the cloud act to stabilize the Arctic stratus (Shupe et al., 2008). This facilitates the simultaneous existence of both phases (Korolev, 2007). Arctic mixed-phase clouds are characterized by such distinct up- and downdraft regions. While in updrafts liquid and ice crystals grow, the cloud top cooling induces downward vertical motion, where Wegener-Bergeron-Findeisen process may dominate. Therefore, these small-scale structures can be important to understand the microphysical processes. However, mixed-phase Arctic stratus typically shows microphysical properties that are inhomogeneous, often on horizontal and vertical scales of a few kilometers and even tens of meters (Chylek and Borel, 2004; Lawson et al., 2010). The small-scale cloud structures, which accompany cloud inhomogeneities, lead to three-dimensional (3D) radiative effects (Varnai and Marshak, 2001). Those can be parameterized using inhomogeneity parameters (Iwabuchi and Hayasaka, 2002; Oreopoulos and Cahalan, 2005).

Unfortunately, the understanding of Arctic clouds is impeded by a paucity of comprehensive observations due to a lack of basic research infrastructure and the harsh Arctic environment (Intrieri et al., 2002; Shupe et al., 2011). Therefore, also observation of small scale cloud structures within the Arctic circle are sparse. Satellite observations are typically too coarse to resolve scales below 250 m. Also, space-born passive remote sensing observations suffer from contrast problems over highly reflecting surfaces (snow and ice, Rossow and Schiffer, 1991). Ground-based remote sensing observations with Radar and LiDAR (Light Detecting And Ranging) typically point only in zenith direction and are not capable to provide the horizontal 2D-structure of clouds. Only along the wind direction the variability of clouds is resolved (Shiobara et al., 2003; Marchand et al., 2007). For example, using correlation analysis, Hinkelmann (2013) revealed significant differences between along-wind and cross-wind solar irradiance variability on small spatial scales in broken-cloud situations. Airborne spectral imaging observation of reflected solar radiation provide measurements with spatial resolution down to several meters. Bierwirth et al. (2013) used airborne measurements of reflected solar spectral radiance to retrieve fields of cloud optical thickness τ of Arctic stratus and demonstrated their strong spatial variability. From similar measurements, Schäfer et al. (2017a) analyzed the directional variability of different cloud types including Arctic stratus. The few analyzed cases show, that 1D-statistics are not sufficient to quantify the variability of horizontal clouds inhomogeneities.

Global reanalysis products have relatively coarse spatial resolutions (40 km and larger; Lindsay et al., 2014) and therefore do not resolve small-scale features. Furthermore, in numerical weather prediction models and climate models, areas of up- and downdrafts in Arctic stratus that are typically in the range of less than 1 km cannot be resolved but have to be parametrized (Field et al., 2004; Klein et al., 2009). To realistically simulate the spatial structure of these clouds, Large Eddy Simulations (LES) with grid spacings of 100 m or less are needed. Thus, these simulations have a high horizontal and vertical resolution, which are important to properly simulate the cloud top structures. Previous LES studies focus for instance on cloud-top entrainment (Mellado, 2017) and emphasize for instance the behavior of changes in the resolution on the liquid water path (Pedersen et al., 2016). Moreover, a high ratio of horizontal grid spacing to vertical grid spacing, called grid aspect ratio, lead to a better agreement with observations. In Kopec et al. (2016) two main processes, radiative cooling and wind shear, are discussed. In their study, radiative cooling sharpened the inversion and wind shear at the top of the atmospheric boundary layer (ABL) is the cause of the turbulence in the capping inversion and lead to dilution at the cloud top. Thus in general, LES are helpful to focus on a certain process and to investigate cloud formation, cloud evolution or the small-scale structures in an Arctic



stratus under controlled conditions. Mixed-phase clouds are challenging for models because of the metastable coexistence of liquid cloud droplets and ice particles. Moreover, the thermal–infrared cooling at cloud top is crucial for the persistence of Arctic stratus (Morrison et al., 2012). Studies have shown that the representation of the temporal evolution of these clouds in numerical weather prediction models and climate models is poor (Barrett et al., 2017a, b). Thus, LES studies are needed to better represent the relevant processes within Arctic mixed-phase clouds.

Here, results from the COSMO (COntortium for Small-Scale MOdeling) model, which is adjusted to a LES setup with a high horizontal and vertical resolution to resolve the cloud structures of Arctic stratus (Loewe et al., 2017; Stevens et al., 2017) are evaluated. For that, data measured by dropsondes served as input for semi–idealized simulations of clouds using COSMO-LES (Sec. 2.3 and Sec. 3). Airborne measured fields of cloud optical thickness retrieved from imaging spectrometer measurements (Sec. 2.2) are used for a comparison with the resulting COSMO clouds with respect to their overall cloud inhomogeneity and directional features of the cloud inhomogeneities (Sec. 4 and Sec. 5). Observations and modelling are aimed to be combined to quantify the horizontal cloud top structures, which are discussed in Sec. 5 and Sec. 6.

2 Airborne measurements

2.1 VERTICAL Distribution of Ice in Arctic clouds (VERDI) campaign

Cloud remote sensing and atmospheric profiles by dropsondes from the airborne VERDI campaign (Bierwirth et al., 2013; Schäfer et al., 2015, 2017a) conducted in April/May 2012 are exploited in this study. VERDI was based in Inuvik, Canada. All data were observed aboard the Polar 5 research aircraft of the Alfred–Wegener–Institute, Helmholtz Centre for Polar and Marine Research (AWI). The measurement flights were mainly carried out in the region over the Beaufort Sea, which was mostly covered by sea ice but also included sea-ice free areas (Polynias). Mostly stratiform low level liquid and mixed-phase clouds within a temperature range of -19°C to 0°C were investigated (Costa et al., 2017). Here, the analysis is focused on a persistent cloud layer probed on four consecutive days from 14 to 17 May 2012. The applied measurements were performed in close vicinity (≤ 50 km) over constant surface conditions (open water; Polynias). The persistent cloud layer in the respective area dissolved continuously from day to day with cloud top altitude decreasing from about 880 m on 14 May to around 200 m on 17 May (Klingebiel et al., 2015; Schäfer et al., 2015, 2017a).

The Polar 5 research aircraft was equipped with a set of cloud and aerosol in situ and remote sensing instruments (Bierwirth et al., 2013; Schäfer et al., 2015; Klingebiel et al., 2015). Atmospheric profiles of temperature, humidity, wind speed and direction were derived from dropsonde measurements, which were regularly released during all flights.

2.2 Horizontal fields of cloud optical thickness

The qualitative and quantitative description of the cloud inhomogeneities is performed using fields of cloud optical thickness τ . Marshak et al. (1995), Oreopoulos et al. (2000), or Schröder (2004) proposed to study horizontal cloud inhomogeneities using cloud-top reflectances. However, Schäfer et al. (2017a) pointed out that radiance measurements include the information of

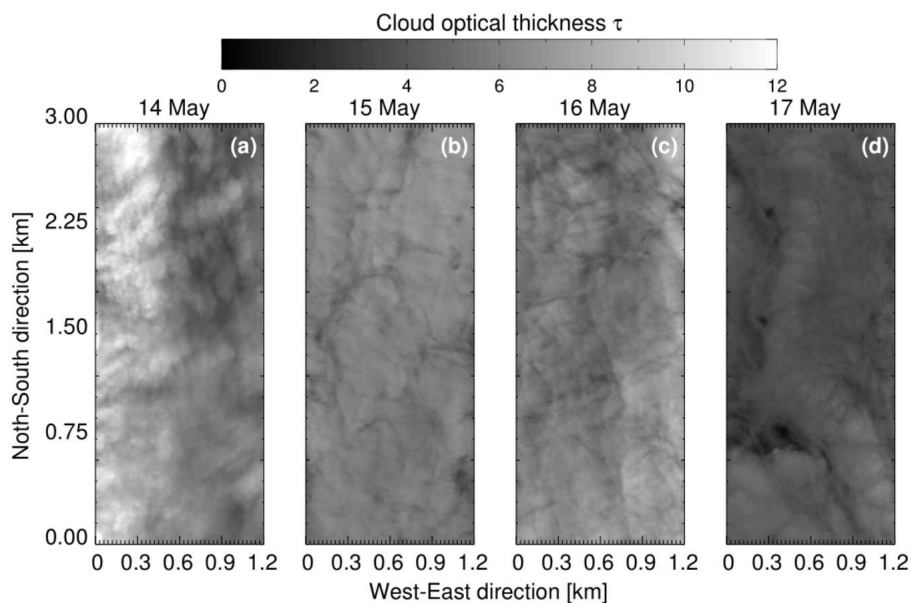


Figure 1. Exemplary depicted sections (1.2 by 3.0 km) of horizontal fields of τ to illustrate the daily variability of the horizontal cloud inhomogeneities during the VERDI campaign on (a) 14 May 2012, (b) 15 May 2012, (c) 16 May 2012, and (d) 17 May 2012. Data adapted from Schäfer et al. (2017b).

the scattering phase function (e.g., forward-/backward scattering peak, halo features). To avoid artifacts in the inhomogeneity analysis from such features, parameters that are independent of the directional scattering of the cloud particles have to be analysed. Therefore, to characterize the observed and simulated cloud fields regarding their horizontal cloud inhomogeneities the cloud optical thickness is applied, which does not include the fingerprint of the scattering phase function.

5 The 2D fields of τ used for the comparison with COSMO are retrieved from 2D fields of reflected solar spectral radiance, which were collected with the imaging spectrometer AisaEAGLE (Schäfer et al., 2013, 2015). Using those data, Schäfer et al. (2017a) retrieved ten fields of cloud optical thickness τ (data set published on PANGAEA, Schäfer et al., 2017b). From those available ten fields of τ , four cases are selected for the comparison to the LES results obtained from COSMO. Figure 1
10 exemplarily illustrates selected sections (1.2 by 3.0 km) of the four chosen cases. The full widths and lengths of the applied fields of τ range to up to 1.7 km and 26.8 km, respectively. Their spatial resolution is 2.6 to 3.6 m (depending on the distance between aircraft and cloud).

During the time period from 14 to 17 May 2012, τ decreased from 8.1 ± 1.2 to 4.3 ± 0.4 (compare Tab. 2, Schäfer et al., 2017a). The selected sections in Fig. 1 illustrate the influence of the temporal evolution on the cloud features. In particular, from 15 to 17 May 2012 a reduction of the horizontal cloud inhomogeneity occurs, which is confirmed by Schäfer et al. (2017a).

15 They also found a continuous reduction of cloud inhomogeneity during those four consecutive days. Furthermore, directional

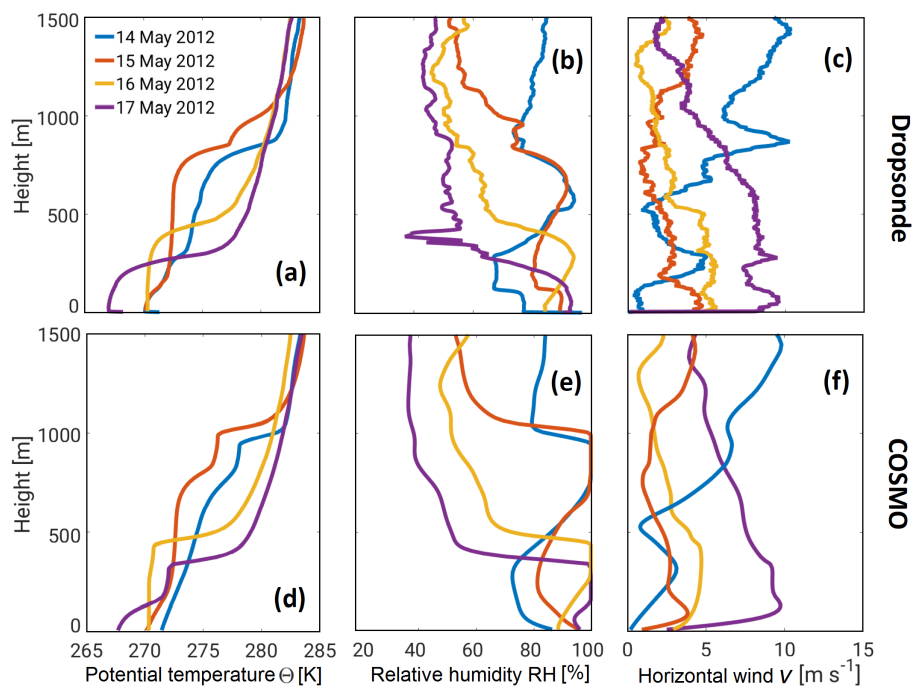


Figure 2. (a, d) Potential temperature (Θ), (b, e) relative humidity (RH), and (c, f) wind speed (v) for the four investigated cases. The dropsonde data is shown in the first row (a-c) and the 2 h domain-averaged profiles after spin-up time of the simulations are shown in the second row (d-f). Dropsondes were released closest to the imaging spectrometer measurements.

features, which are prominent on 14 May, seem to be reduced, which is confirmed by autocorrelation analysis performed by Schäfer et al. (2017a).

2.3 Atmospheric profiles

During each measurement flight Vaisala dropsondes (type RD94) were used together with the Vaisala AVAPS (Airborne Vertical Atmosphere Profiling System) dropsonde receiving system (Hock and Franklin, 1999; Coleman, 2003). The dropsondes were released to sample profiles of meteorological parameters (air pressure p , air temperature T , relative humidity RH , wind speed v , and wind direction WD) below the aircraft, which then was typically operating at about 3 km altitude and allowed to sample the entire cloud and ABL structure by the dropsondes. The accuracy of the dropsonde measurements is given by the manufacturer and specified to ± 0.4 hPa for the air pressure, $\pm 0.2^\circ\text{C}$ for the air temperature, $\pm 2\%$ for the relative humidity, and ± 0.5 m s^{-1} for the detected wind speed. For the analysis of the cloud fields, the dropsonde releases closest to the four investigated remote sensing observations had been chosen. The potential temperature (Θ), relative humidity (RH), and wind speed (v) profiles for the four investigated cases are displayed in Fig. 2. From 14 May to 15 May the cloud top inversion increased from 810 m to 880 m while for the subsequent two days, the inversion layer decreased to 440 m on 16 May and to



200 m on 17 May 2012. In conjunction with the decrease of the cloud top altitude the cloud base altitude decreased as well until it almost reached the surface on 17 May. The relative humidity, displayed in Fig. 2b confirms the initial increase and consecutive decrease of the cloud top and base altitude. The inversion strength increased over the time period from ≈ 5 K to ≈ 1 K mainly because the temperature of the surface layer continuously decreased; the ABL became more stable.

5 Furthermore, Fig. 2c illustrates that the near-surface wind increased during the four days from ≈ 1 to ≈ 10 m s⁻¹, which might be of interest in terms of the generation of cloud inhomogeneities. Except for the case on 14 May, where wind speeds in higher altitudes are larger compared to the other days, the daily increase of the near-surface wind speed is also observed in higher altitudes to up to 1 km. Following Jacobson et al. (2013), this is related to Low-Level-Jets (LLJ) for the days from 15 to 17 May.

10 3 Simulations

3.1 COSMO: General setup

COSMO is a non-hydrostatic, limited-area atmospheric forecast model (Schättler et al., 2015). Here it is used in a semi-idealized LES setup which follows the description by Loewe et al. (2017), based on Ovchinnikov et al. (2014) and Paukert and Hoose (2014). The size of the model domain is 6.4×6.4 km in horizontal direction with a grid spacing of 100 m. The vertical
15 height range of 22 km is divided into 166 vertical levels, which are concentrated on the ABL with a typical grid spacing of around 15 m. The initialization profiles of temperature, humidity, wind speed, and wind direction are based on the dropsonde data, whereby parts of the original profiles (Fig. 2) are smoothed to avoid numerical issues of the model. Moreover, ERA (European Reanalysis) -Interim reanalysis data (from the European Centre for Medium-Range Weather forecast (ECMWF)) (Dee et al., 2011) have been used to complete the profiles above the altitude where the dropsondes were released. Other model
20 parameters such as the description of the large scale subsidence, which is adjusted to the temperature inversion height, the relaxation to fixed cloud droplet number concentration (CDNC) and ice crystal number concentration (ICNC), and the spin up time of 2 h follows Ovchinnikov et al. (2014). The CDNCs are based on measurements of the Small Ice Detector mark 3 (SID3) measurements (Vochezer et al., 2016). During the four investigated days, CDNC of 90 to 100 cm⁻³ were observed as summarized in Tab. 1. Unfortunately, the concentration of ice crystals was below or at the detection limit of the SID3.
25 Therefore, the ICNC were assumed to be one particle per liter according to observations of mixed-phase Arctic stratus during the Indirect and Semi-Direct Aerosol Campaign (ISDAC) (McFarquhar et al., 2011; Ovchinnikov et al., 2014). The inversion height of the temperature $z(T_{in})$ is necessary for the description of the large scale subsidence in the model and is represented by the inversion height of the dropsonde profiles, which are used for initialization of the model simulations (Tab. 1).

3.2 Domain-averaged cloud properties and temporal evolution

30 Time series of simulated liquid water content (LWC) and ice water content (IWC) for the four selected cases are shown in Fig. 3. During the four flights, which are simulated with COSMO, only few ice crystals were observed. In terms of the model



Table 1. Model setup specifications of the different mixed-phase cloud simulations of four VERDI campaign days.

Case	$z(T_{in})$ [m]	CDNC [cm^{-3}]	ICNC [l^{-1}]
14 May	870	100	1
15 May	988	100	1
16 May	440	90	1
17 May	350	100	1

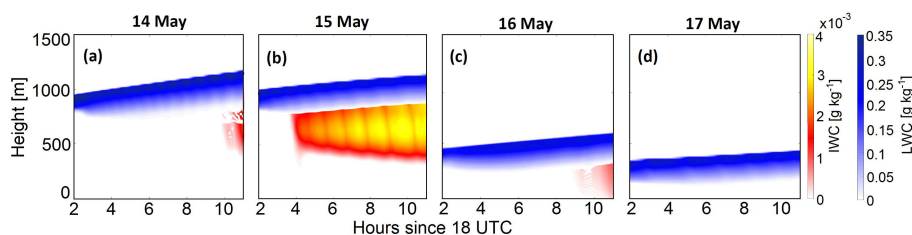


Figure 3. Domain averages of LWC (blue color scale) and IWC (red-yellow color scale) of the four simulations during the VERDI campaign. Please note the different color scale for the IWC in (d).

domain average profiles of the LWC and IWC, the simulated clouds consist mostly of liquid water droplets except for the 15 May, in which more IWC is built from around 4 h on (Fig. 3b). Furthermore, the cloud top is around 1000 m for the 14 May and the 15 May (Fig. 3a, b). However, the cloud top height increases during time in all four simulations because of entrainment of air through the top of the ABL. This is evident in the temporal evolution of LWC, which has a maximum between 0.25 and 0.35 g kg^{-1} near the cloud top. The Arctic clouds on 16 May and 17 May are the lowest simulated clouds with a cloud top initially around 450 m and 350 m, respectively (Fig. 3 c, d).

The four simulations show differences in the temperature, relative humidity and wind speed profiles (Fig. 2d–f), which in general still agree with the initial dropsonde profiles after the spin up time (Fig. 2a–c). The height of the ABLs and the strength of the inversions are lower in the simulations of the 16 May and 17 May. Furthermore, for the simulation on 17 May a second inversion develops in the ABL near the surface around 60 m to 150 m. The ABL structure is well mixed in the simulation of the 16 May although no second temperature inversion is built near the surface. The simulation of the 16 May shows a wind shear from around 150° to around 100° (Fig. 4) and a decrease of v with height above the cloud top height, which is also seen in the dropsonde profiles (Fig. 2c and Fig. 4). The other simulations do not show a turning of the wind above the inversion height.

The simulated mixed-phase clouds of the four VERDI flights show a liquid water path (LWP) around 35 to 50 g m^{-2} . The highest LWP is seen in the simulation of the 14 May, which increases towards 50 g m^{-2} at the end of the simulation. The simulation of the 15 May has the lowest LWP values. Furthermore, the LWP remains very stable until the end of the simulation. The ice water path (IWP) and the snow water path (SWP) of all four simulations is small especially for the simulated clouds on the 14, 16, and 17 May, which fits well with observations.

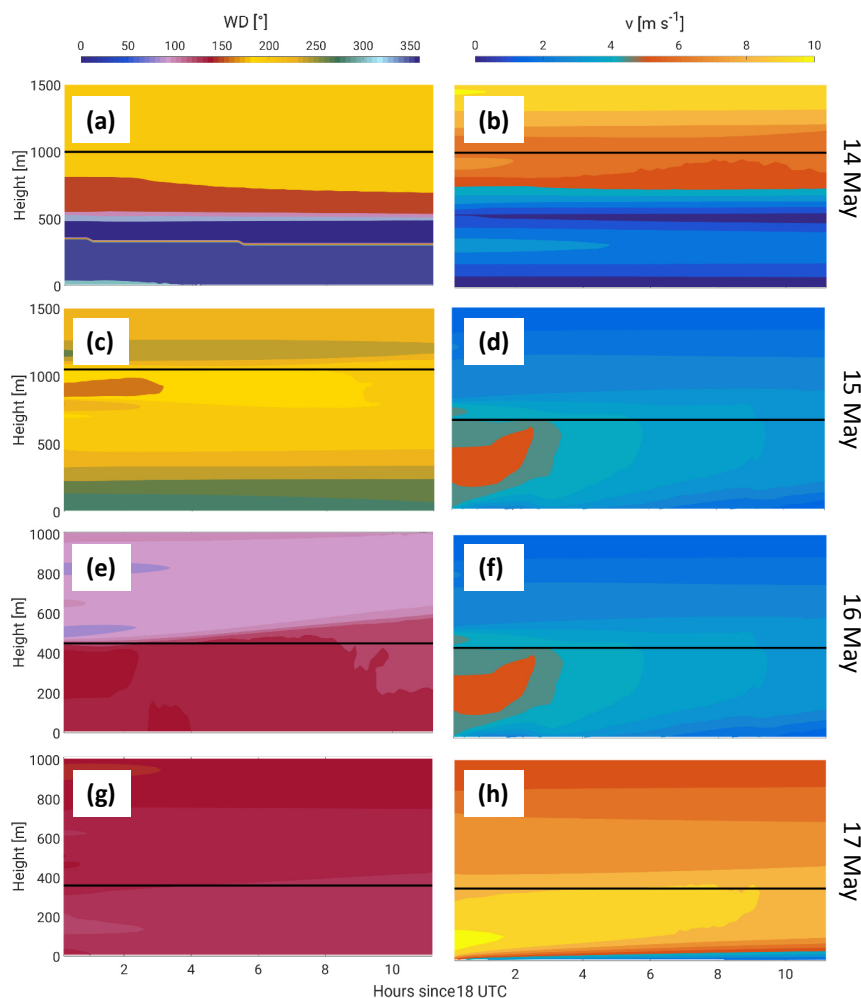


Figure 4. Domain averaged WD (a, c, e, g) and v (b, d, f, h) of the four VERDI simulations. The black line marks the averaged cloud top height during the simulation.

For the comparison of the simulated and observed horizontal cloud structures (cloud inhomogeneities), fields of simulated cloud optical thickness (τ_{sim}) are compared to retrieved fields of cloud optical thickness from the measurements (τ_{meas}). The τ_{sim} is calculated within the COSMO model considering the amount of liquid water and the solar spectrum. However, it cannot be expected that COSMO is capable of reproducing the detailed spatial and temporal cloud evolutions, which are captured by the observed fields of τ , accurately (inhomogeneity features and directional structures). Therefore, besides the comparison of observed and simulated clouds with regard to macrophysical cloud features (cloud vertical extent, cloud optical thickness) of the individual cases, instead of point-by-point comparisons of cloud parameters, statistical bulk parameters describing the horizontal cloud inhomogeneities, their directional structures, and the temporal evolution of both will be compared.



4 Quantification of cloud inhomogeneities

4.1 One-dimensional statistical bulk parameters

For the quantitative description of the cloud inhomogeneities from the simulated fields of cloud optical thickness (τ_{sim}) obtained from COSMO and measurement-based retrieved fields of cloud optical thickness (τ_{meas}) collected during the VERDI campaign, 5 statistical techniques are applied. Following Schäfer et al. (2017a), different statistical quantitative measures of the cloud inhomogeneities are derived using the mean and standard deviation of the particular τ field and three 1D inhomogeneity parameters ρ_τ (Davis et al., 1999b; Szczap et al., 2000), S_τ (Davis et al., 1999b; Szczap et al., 2000), and χ_τ (Cahalan, 1994; Oreopoulos and Cahalan, 2005). They are given by:

$$\rho_\tau = \frac{\sigma_\tau}{\bar{\tau}}, \quad (1)$$

10

$$S_\tau = \frac{\sqrt{\ln(\rho_\tau^2 + 1)}}{\ln 10}, \quad (2)$$

$$\chi_\tau = \frac{\exp(\ln \bar{\tau})}{\bar{\tau}}. \quad (3)$$

A homogeneous cloud is characterized by $\rho_\tau = 0$ and $S_\tau = 0$. Higher values of ρ_τ and S_τ indicate more pronounced cloud 15 inhomogeneity. However, both of them have no predefined upper limit. Therefore, ρ_τ and S_τ only sustain a quantitative significance, when their values for different cases are compared to each other. The 1D inhomogeneity parameter χ_τ ranges between 0 and 1, with values close to unity indicating horizontal homogeneity and values approaching zero characterizing high horizontal inhomogeneity. Due to the limited range between 0 and 1, χ_τ is not only a qualitative but also quantitative measure.

4.2 Two-dimensional autocorrelation analysis

20 Two-dimensional autocorrelation analysis is applied to quantify the typical scales of cloud inhomogeneities and to identify directional patterns of the cloud structure (Schäfer et al., 2017a). To derive the autocorrelation functions, each field of τ is correlated with itself, while it is shifted pixel by pixel (observations) or grid point by grid point (simulations) against itself. The values of the resulting correlation coefficients after each shift are in the range between -1 (perfect negative correlation) and 1 (perfect positive correlation). Correlation coefficients with values of 0 identify no correlation. Here, only the degree of 25 correlation matters, not if it has a positive or negative sign. Similar to Schäfer et al. (2017a), squared autocorrelation functions P_τ^2 are used to avoid ambiguous interpretations. The P_τ^2 reach values between 0 (no correlation) and 1 (perfect correlation). The particular correlation coefficients at the derived distances identify the similarity of the horizontal cloud structures. If the cloud is horizontally homogeneous, the correlation coefficients stay constant over large distances. If the cloud is rather inhomogeneous the correlation coefficients already drop at closer distances. Therefore, P_τ^2 as a function of distances is a measure 30 of the size of the dominant cloud structures.



A quantitative value for the distance at which cloud structures are different from each other (namely decorrelated) is the decorrelation length ξ_τ (Schäfer et al., 2017a). It is the distance at which P_τ^2 drops to:

$$P_\tau^2(\xi_\tau) = \frac{1}{e^2}. \quad (4)$$

In a 2D-autocorrelation function, ξ_τ can differ depending on the orientation, if the cloud structures have a predominant orientation. To quantify this directionality, ξ_τ is calculated along (ξ_τ^\updownarrow) and across ($\xi_\tau^{\leftrightarrow}$) the predominant direction. The larger the differences between ξ_τ^\updownarrow and $\xi_\tau^{\leftrightarrow}$, the more cloud structures are orientated.

Figure 5a shows a section of an observed field of τ_{meas} , retrieved from the measurements on 15 May. The depicted section has a swath of 1.3 km (oriented in y direction) and a length of 6 km (oriented in x direction). Figure 5b shows the corresponding field of τ_{sim} (6 km \times 6 km, adapted to the selected length of the measurement case), which is simulated with COSMO two hours after the spin up time for the case on 15 May. For comparability reasons, both fields of τ are normalized by their maximum.

Although the swath (y direction) of the field of τ_{meas} is smaller by a factor of almost five compared to the field of τ_{sim} , larger cloud structures of similar size and shape are obvious in both fields of τ_{meas} and τ_{sim} . However, with 488 spatial pixels along the swath (spatial double binning was applied during measurements) and a field of view of 37° AisaEAGLE's spatial resolution is ≈ 1.3 m for a target in a distance of 1 km. Thus, the spatial resolution of AisaEAGLE is relatively large, compared to the grid spacing of 100 m from COSMO. Thereby, the exact pixel size of AisaEAGLE depends on the distance between aircraft and cloud, which leads to pixel sizes between 2.6 and 3.6 m. Due to the 30 to 40 times higher resolution of AisaEAGLE, compared to COSMO's grid spacing, the measurements shows cloud features, which cannot be resolved by COSMO. Those features on a spatial scale below 100 m may have an effect on the statistical (1D inhomogeneity parameters) and spatial comparison (autocorrelation analysis) of the particular fields of τ .

To quantify the size and orientation of the represented cloud structures in the observations and simulations, Fig. 5c and Fig. 5d show the calculated squared 2D autocorrelation coefficients P_τ^2 . To calculate them, different numbers of legs (shifts) have to be applied for $P_{\tau,\text{meas}}^2$ and $P_{\tau,\text{sim}}^2$. The applied field of τ_{meas} consists of 2700×450 spatial pixels. Therefore, restricted to the shorter side, 225×225 (half of swath pixel number, calculated into x and y direction) legs are chosen for the calculation of the 2D $P_{\tau,\text{meas}}^2$. COSMO consists of 64×64 grid points. This allows 32×32 legs for the calculation of $P_{\tau,\text{sim}}^2$.

The resolved domain and pixel/grid-point sizes displayed in Fig. 5c and Fig. 5d show significant differences, which reveals that a direct comparison is difficult. Applying the 2D autocorrelation analysis to the observations allows to resolve small-scale cloud structures with high spatial resolution (≈ 2.7 m), but only within a narrow spatial range below 1 km. Contrarily, the same analysis for COSMO delivers $P_{\tau,\text{sim}}^2$ with lower resolution (≥ 100 m), but over a larger spatial range (≤ 3.2 km, in Fig. 5d only displayed until 2 km). Thus, also large-scale cloud structures are covered by COSMO (purple stripes in Fig. 5d) but not in the observations. Therefore, to make a direct comparison possible, the spatial sizes (pixel/grid point size, domain size) of both datasets need to be conformed.

Furthermore, both, Fig. 5c and Fig. 5d show predominant directional features of the cloud structures. Their lengths and widths are derived from 1D autocorrelation functions along (straight white line in Fig. 5c and Fig. 5d) and across (dashed white line in Fig. 5c and Fig. 5d) those predominant directional structures and a subsequent estimation of ξ_τ^\updownarrow and $\xi_\tau^{\leftrightarrow}$. The derived ξ_τ^\updownarrow

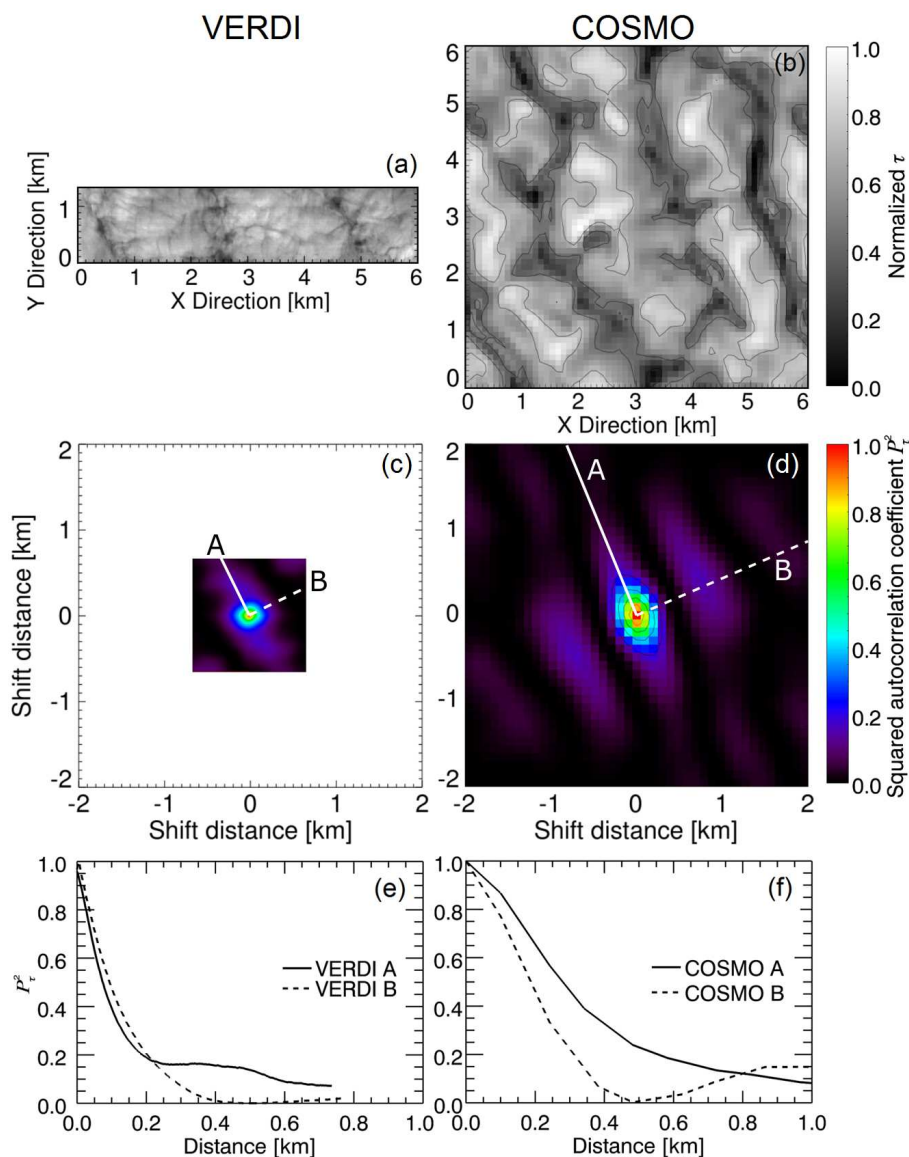


Figure 5. (a–b) Horizontal fields of normalized τ_{meas} (VERDI) and τ_{sim} (COSMO) for the case on 15 May 2012. (c–d) Two-dimensional autocorrelation coefficients $P_{\tau, \text{meas}}^2$ and $P_{\tau, \text{sim}}^2$, calculated for fields of τ displayed in (a) and (b). (e–f) One-dimensional autocorrelation coefficients along (straight white line marked in (c) and (d)) and across (dashed white line marked in (c) and (d)) predominant directional structure. The grey dotted line illustrates the threshold for the estimation of ξ_{τ}^{\downarrow} and $\xi_{\tau}^{\leftrightarrow}$.

and $\xi_{\tau}^{\leftrightarrow}$ show an overall agreement but still differ from each other. For the observations $\xi_{\tau, \text{meas}}^{\downarrow}$ and $\xi_{\tau, \text{meas}}^{\leftrightarrow}$ reach distances of ≈ 500 m and ≈ 250 m, respectively. Contrarily, for the simulations $\xi_{\tau, \text{sim}}^{\downarrow}$ and $\xi_{\tau, \text{sim}}^{\leftrightarrow}$ reach distances of ≈ 800 m and ≈ 400 m,



respectively. This might be a further indication that it is necessary to make the fields of τ_{meas} and τ_{sim} conform with regard to their spatial resolution and domain.

4.3 Final data preparation - Domain adjustment

To compare both data sets, the fields of τ_{meas} , which are retrieved from the imaging spectrometer measurements are averaged
5 to the spatial resolution of the COSMO τ_{sim} fields. In order to do so, the τ_{meas} -values of distinct numbers of neighbouring pixels are averaged. The number depends on the single pixel size of the particular cases, which is a function of the distance between aircraft and cloud. For the four investigated cases this number varies between 26 and 37 pixels, which are needed to generate pixel sizes of τ_{meas} comparable to the 100 m grid spacing of COSMO.

Furthermore, the domain size of the measurements and simulations are different. COSMO's domain size of 6.4 by 6.4 km is
10 about three to four times larger than the domain size of the measurements. Therefore, to compare both data sets, the COSMO domain size is also reduced to the width and length of the corresponding τ_{meas} field from the measurements. Therefore, for the comparison only a squared domain in the center of COSMO's τ_{sim} field is used, which size corresponds to the size of the particular field from the measurement. For the four investigated cases this results in COSMO domains composed out of 12×12 to 16×16 grid points (1.2×1.2 km to 1.6×1.6 km). Longer stripes of τ_{meas} -fields and stripes according to their
15 lengths across the COSMO domain are not used, because the investigations are focused on small scale cloud inhomogeneities, which are already covered by the smaller squared domain size given by the swath of the τ_{meas} -fields.

However, to increase the statistics, which might be otherwise too small because of the finally applied small domain but large pixel sizes, for COSMO averages of the resulting $P_{\tau, \text{sim}}^2$ over all output time steps after spin up are used. For the measured fields, whose lengths are much longer than their widths, squared domains (size determined by swath of τ_{meas}) are cut along the
20 measured stripe and the resulting $P_{\tau, \text{meas}}^2$ are averaged accordingly. Increasing the number of available $P_{\tau, \text{meas}}^2$ to average is a further restriction to use squared domains instead of stripes.

To test possible effects arising from the change of spatial resolution and to check if the relevant scales of cloud inhomogeneity are lost, when reducing the resolution of the measurements, Fig. 6a to Fig. 6e show sections of one and the same field of τ_{meas} from 14 May, but displayed with a different spatial resolution of 3 m (original resolution), 30 m, 100 m (COSMO resolution),
25 150 m, and 300 m resolution. Figure 6f to Fig. 6j show the corresponding squared 2D autocorrelation coefficients. The red line illustrates the direction, which is used to calculate the squared 1D autocorrelation functions and decorrelation lengths ξ_{τ} displayed in Fig. 6k to Fig. 6o. The fields from the 2D autocorrelation analysis show that except for the spatial resolution of 300 m the directional structure of the cloud inhomogeneities is still captured, when the spatial resolution is reduced. However, the decorrelation lengths, derived from the 1D autocorrelation analysis increases with decreasing spatial resolution from
30 $\xi_{\tau} = 327$ m at 3 m spatial resolution to $\xi_{\tau} = 600$ m at 300 m spatial resolution. Therefore, decreasing spatial resolution leads to larger ξ_{τ} , which indicates larger cloud structures. This means that reduced spatial resolution will generate fields of τ with larger spatial scales.

To test the influence of the spatial resolution on the overall inhomogeneity, Fig. 7a shows the results for the mean and standard deviation of the fields of τ , illustrated in Fig. 6. Figure 7b shows the corresponding 1D inhomogeneity parameters ρ_{τ} and

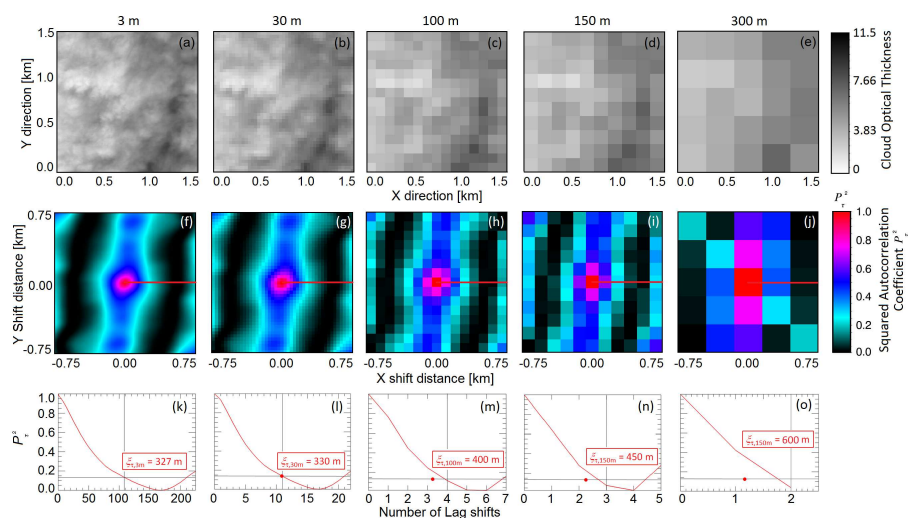


Figure 6. Illustrated are sections of one and the same field of τ_{meas} from 14 May 2012 with a spatial resolutions of (a) ≈ 3 m (original resolution), (b) 30 m, (c) 100 m (COSMO resolution), (d) 150 m, and (e) 300 m. (f–j) Squared 2D autocorrelation coefficients P_{τ}^2 calculated for the fields of τ_{meas} displayed in (a) to (e). (k–o) Squared 1D autocorrelation coefficients P_{τ}^2 calculated along straight red line in (f) to (j). Estimated decorrelation length ξ_{τ} is marked by horizontal and vertical black line and labeled by its value. Red dot marks ξ_{τ} as derived from the case with the original spatial resolution of 3 m.

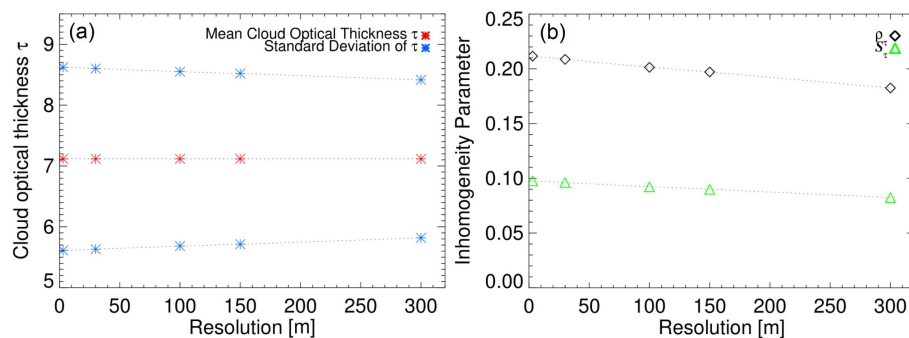


Figure 7. Comparison of (a) mean and standard deviation and (b) inhomogeneity parameters ρ and S as a function of spatial resolution for the fields of τ_{meas} illustrated in Fig. 6a–e.

S_{τ} . While the mean value of τ stays constant for all spatial resolutions, its standard deviation decreases with increasing pixel size. This indicates that the fields of τ become more homogeneous the larger the pixel size is. Comparably, the value of both 1D inhomogeneity parameters ρ_{τ} and S_{τ} decrease with increasing pixel size, which further confirms the reduction of the inhomogeneity.



Table 2. Mean value of τ , standard deviation σ_τ , and the three 1D inhomogeneity parameters ρ_τ , S_τ , and χ_τ calculated for all four cases from the observations and simulations.

	Case	$\bar{\tau} \pm \sigma_\tau$	ρ_τ	S_τ	χ_τ
VERDI	14 May	8.1 ± 1.2	0.209	0.093	0.977
	15 May	6.4 ± 0.5	0.115	0.052	0.993
	16 May	6.6 ± 0.6	0.145	0.065	0.988
	17 May	4.3 ± 0.4	0.132	0.061	0.990
COSMO	14 May	6.9 ± 0.5	0.066	0.028	0.997
	15 May	5.4 ± 0.3	0.053	0.023	0.998
	16 May	5.5 ± 0.5	0.090	0.037	0.996
	17 May	5.6 ± 0.3	0.044	0.019	0.999

5 Comparison of modeled against observed cloud structures

5.1 Magnitude of inhomogeneity

The fields of τ obtained from the spectral imaging remote sensing (τ_{meas}) are compared to the fields of τ derived from the COSMO simulations (τ_{sim}). To validate the cloud inhomogeneity in the simulated fields, the statistical techniques from Sect. 4.1 including the averaging of the measured fields to 100 m pixel size are applied. Tab. 2 lists the mean value of τ , standard deviation σ_τ , and the three 1D inhomogeneity parameters ρ_τ , S_τ , and χ_τ for the simulations and observations.

Both, measurements and simulation show the highest cloud optical thickness on 14 May with $\bar{\tau}_{\text{meas}} = 8.1 \pm 1.2$ and $\bar{\tau}_{\text{sim}} = 6.9 \pm 0.5$, which show an overall agreement. During the course of the following days, the large scale subsidence lead to a decrease of the cloud top altitude and cloud geometrical thickness and corresponding lower values of τ and σ_τ . For these days, model and observations are still in agreement.

Regarding the cloud inhomogeneity, the absolute values of the 1D inhomogeneity parameters ρ_τ , S_τ , and χ_τ do not compare well. The results for the COSMO simulations show lower 1D inhomogeneity parameters (more homogeneous) by a factor of two and higher, compared to the results from the measurements. The comparably lower inhomogeneity derived from COSMO might be caused by its effective grid spacing, which is approximately three times 100 m (Skamarock et al., 2011). Although the pixel size of AisaEAGLE is adapted to the COSMO grid spacing by averaging over neighboring pixels, COSMO's effective grid spacing is larger, which might lead to larger homogeneity of the simulations compared to the observations. Furthermore, COSMO simulates the cloud at the same location, where it is initialized. Contrarily, the AisaEAGLE measurements took place along a stripe of several kilometers. The simulated clouds may not change in between the time steps as much as the measurements of the clouds along the measurement stripe do. Therefore, averaging over COSMO's time steps might produce more homogeneous results than averaging over AisaEAGLE's squared domains along the flight track.

However, the observations show that the cloud field became more homogeneous from 14 to 15 May as indicated by lower



values of ρ_τ (ρ_τ reduces from 0.209 to 0.115). From 15 to 16 May ρ_τ increases to 0.145, which indicates a cloud field with slightly higher inhomogeneity. Then, on 17 May ρ_τ reduced to 0.132, showing that the cloud field became more homogeneous again. This trend is reproduced by the COSMO results, except that ρ_τ increases to larger values on 16 May than on 14 May, which is not seen from the observations.

- 5 This trend of decreasing/increasing inhomogeneity is also imprinted in the inhomogeneity parameters S_τ and χ_τ , which decrease/increase with time in both, measurements and simulations. In this regard, COSMO performs well.

5.2 Spatial inhomogeneity scale

The 2D autocorrelation functions are calculated to compare the typical spatial scales and the directional character of the cloud inhomogeneities of observations and simulations. The 2D autocorrelation coefficients ($P_{\tau,\text{meas}}^2$; $P_{\tau,\text{sim}}^2$) for each case are shown in Fig. 8e to Fig. 8h for the measurements and in Fig. 8m to Fig. 8p for the simulations. Additionally, representative fields of normalized τ_{meas} (Fig. 8a–d) and τ_{sim} (Fig. 8i–l) are added. The 2D autocorrelation analysis was applied to the simulated fields of τ_{sim} orientated in a North-South and West-East grid. The orientation of the observations is determined by the flight direction. Therefore, the orientation of the fields of τ_{meas} and $P_{\tau,\text{meas}}^2$ are rotated into the direction of the COSMO grid. One-dimensional P_τ^2 are calculated manually along the dominant direction (straight red and blue lines in Fig. 8e–h and Fig. 8m–p) and across (dashed red and blue lines in Fig. 8e–h and Fig. 8m–p) it. For $P_{\tau,\text{meas}}^2$ (red) and $P_{\tau,\text{sim}}^2$ (blue) the results are displayed in Fig. 8i to Fig. 8l. The dotted black line illustrates the threshold for the estimation of ξ_τ .

The observations on 14 May are influenced by a large scale cloud structure, which is caused by large scale dynamic forcing and leads to an increase of the autocorrelation coefficients for distances larger than 700 m. Furthermore, during this day a significant directional structure from North–West to South–East is observed. Along this direction the cloud field stays homogeneous over a wide range ($\xi_\tau = 700$ m). Across this predominant structure the small-scale cloud structures reach a decorrelation length of $\xi_\tau = 300$ m. During the following days the orientation of the directional structure turns eastwards in the observations and the difference between ξ_τ^\updownarrow and $\xi_\tau^{\leftrightarrow}$ decreases. This characterizes a weakening of the directional structure of the cloud field. Only on 16 May a directional orientation can be identified, while on 15 and 17 May the clouds are characterized by a rather indifferent horizontal structure.

Comparing the results for $P_{\tau,\text{sim}}^2$ with $P_{\tau,\text{meas}}^2$ reveals that the large scale cloud structure is not simulated for the case on 14 May. This results most probably from the small domain size of COSMO, which is fixed over the same location when averaging the $P_{\tau,\text{sim}}^2$ over a set of time steps. Contrarily, the averages of $P_{\tau,\text{meas}}^2$ from the measurements are performed over a set of squared domains along the flight track. Thus, the chance to cover also larger structures is higher for the measurements compared to the simulations. However, the influences of the large scale cloud structures on the decorrelation length ξ_τ of the small scale cloud inhomogeneities is low and can be neglected.

Furthermore, the results for $P_{\tau,\text{meas}}^2$ and $P_{\tau,\text{sim}}^2$ show that COSMO produces larger small-scale cloud structures compared to the measurements. In Fig. 8m to Fig. 8p the covered areas of $P_{\tau,\text{sim}}^2$ are larger compared to the areas covered by $P_{\tau,\text{meas}}^2$ in Fig. 8e to Fig. 8h. Table 3 lists the resulting $\xi_{\tau,\text{meas}}$ and $\xi_{\tau,\text{sim}}$ calculated along (ξ_τ^\updownarrow) and across ($\xi_\tau^{\leftrightarrow}$) the predominant structures found in

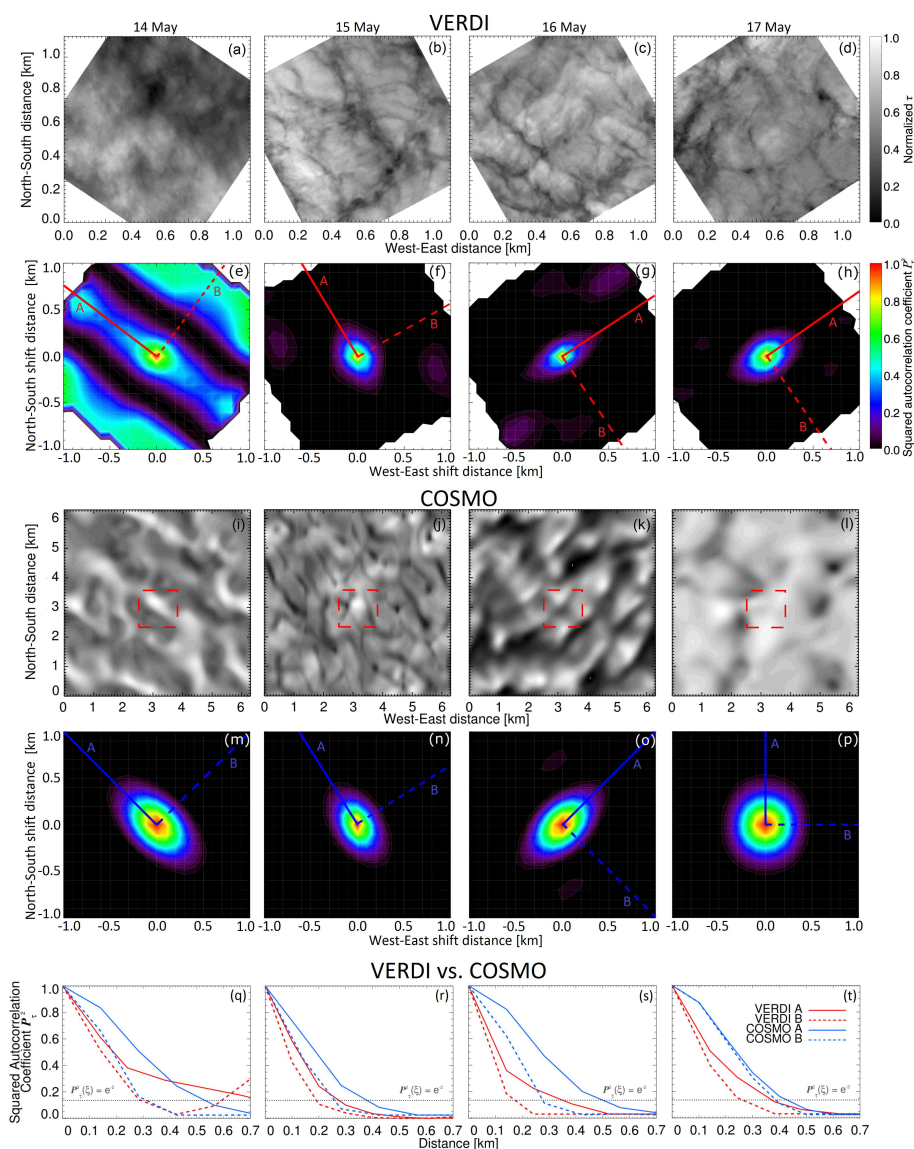


Figure 8. (a-d) Exemplary depicted sections of fields of τ_{meas} observed during VERDI from 14 to 17 May 2012. (e-h) Mean 2D autocorrelation coefficients $P_{\tau_{\text{meas}}}^2$ derived for fields of τ_{meas} from VERDI. (i-l) Exemplary depicted fields of τ_{sim} simulated with COSMO for the VERDI cases from 14 to 17 May 2012. Dashed red boxes illustrate corresponding domain of observed fields of τ_{meas} . (m-p) Mean 2D autocorrelation coefficients $P_{\tau_{\text{sim}}}^2$ derived for fields of τ_{sim} . (q-t) Decorrelation length ξ_{τ} along strongest (straight blue and red lines) and weakest (dashed blue and red lines) extend of 2D autocorrelation coefficients derived from $P_{\tau_{\text{meas}}}^2$ in (e-h) and $P_{\tau_{\text{sim}}}^2$ in (m-p), respectively.

Fig. 8e-h and Fig. 8m-p. A comparison reveals differences between $\xi_{\tau_{\text{meas}}}$ and $\xi_{\tau_{\text{sim}}}$. The values from the simulations (except for ξ_{τ}^{\uparrow} on 14 May) are larger compared to the values from the observations by 20 to 30 %.



Table 3. For all four cases from the observations and simulations calculated decorrelation lengths $\xi_{\tau, \text{meas}}$ and $\xi_{\tau, \text{sim}}$ along (ξ_{τ}^{\downarrow}) and across ($\xi_{\tau}^{\leftrightarrow}$) the predominant directions found in Fig. 8e–h and Fig. 8m–p.

	Case	ξ_{τ}^{\downarrow} [m]	$\xi_{\tau}^{\leftrightarrow}$ [m]
VERDI	14 May	700	290
	15 May	280	190
	16 May	350	170
	17 May	370	260
COSMO	14 May	530	320
	15 May	380	260
	16 May	500	280
	17 May	430	390

However, the $P_{\tau, \text{sim}}^2$ follow the trend, which is observed for $P_{\tau, \text{meas}}^2$, including their predominant directional structure. Like for the measurements on 14 May a predominant North–West to South–East direction is simulated, which then turns eastwards. Thereby, the cases on 14 May and 16 May show the strongest directional features (largest differences between ξ_{τ}^{\downarrow} and $\xi_{\tau}^{\leftrightarrow}$). Although on 17 May COSMO simulates a more isotropic structure ($\xi_{\tau}^{\downarrow} \approx \xi_{\tau}^{\leftrightarrow} \approx 400$ m) of the cloud inhomogeneities compared to the measurements ($\xi_{\tau}^{\downarrow} = 370$ m \neq $\xi_{\tau}^{\leftrightarrow} = 260$ m) it captures the reduction of the overall directionality. Therefore, the overall results with regard to the directional structure provided by COSMO are acceptable.

6 Sensitivity Study

The reasons for the differences on 16 May are related to the wind field and the temperature profile. Figure 4e and Fig. 4f illustrate a development of the wind profile in the simulations with simulation time. While the wind direction does not change at the cloud top of the 14, 15, and 17 May, the simulation of the 16 May shows a turning of the wind. Together with the well-mixed ABL (Fig. 2) this case shows a typical example of a cold air outbreak roll convection (e.g., Brümmer, 1999). On 16 May the simulated wind speed is significantly higher compared to the other days, resulting from the initial conditions in the dropsonde profile. However, since the wind speed, wind direction, and temperature profile are the only parameters which have been changed in the model input, the wind speed and wind shear are expected to be main drivers for the degree of horizontal cloud inhomogeneity.

To test its influence on the horizontal cloud inhomogeneity, the simulation for 15 May is repeated for different initializations, where the wind profile was varied. Based on the original wind profile, the wind speeds at each altitude are multiplied by (a) 0.5, (b) 1.0, (c) 1.5, (d) 2.0, (e) 2.5, and (f) 3.0. This leads to mean wind speeds (vertically averaged over cloudy region) of (a) ≈ 0.7 m s⁻¹, (b) ≈ 1.5 m s⁻¹, (c) ≈ 2.2 m s⁻¹, (d) ≈ 3.0 m s⁻¹, (e) ≈ 3.7 m s⁻¹, and (f) ≈ 4.4 m s⁻¹. The wind shear was kept constant throughout all simulations.

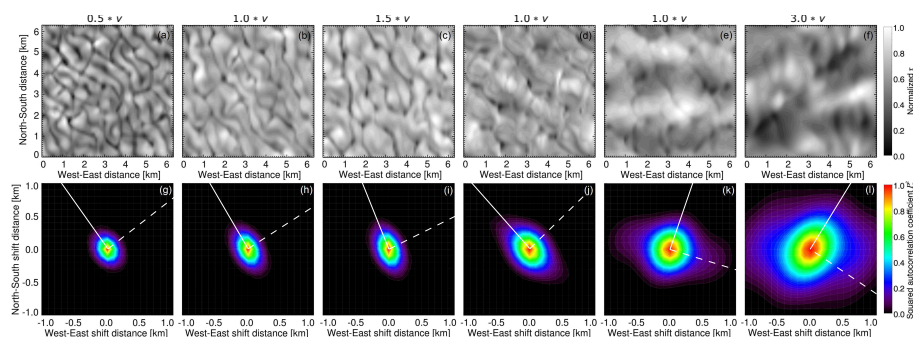


Figure 9. (a)–(f) Exemplary depicted fields of τ_{sim} for the 15 May 2012 case simulated with differently scaled initial wind speeds. (g)–(i) Calculated 2D autocorrelation coefficients P_{τ}^2 for case (a)–(f). Additionally, white lines illustrate the orientation used for the calculation of the 1D P_{τ}^2 along (straight white lines) and across (dashed white lines) the dominant directions illustrated in Fig. 10.

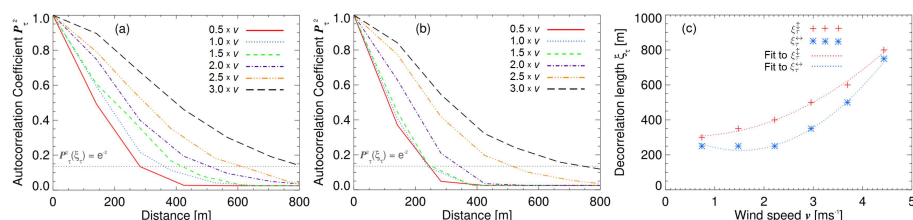


Figure 10. For the six cases of different wind speed calculated 1D autocorrelation functions (a) along and (b) across the main structures, identified in Fig. 9(g)–(i). The grey dotted line marks the threshold of $P_{\tau}^2(\xi_{\tau}) = e^{-2}$. (c) From (a) and (b) derived discrete values for the decorrelation lengths ξ_{τ}^{\uparrow} and ξ_{τ}^{\rightarrow} as a function of wind speed v (symbols). Additionally included are fits derived from Eq. (5) and Eq. (6) (dotted lines).

Figure 9a to Fig. 9f show the simulated 2D fields of τ_{sim} (6.4×6.4 km, 100 m spatial resolution). Small-scale structures (≤ 0.5 km) are obvious. For lower wind speeds, these small scale structures have a North–West to South–East orientation, which turns into North–East to South–West orientation with increasing wind speeds. Large-scale structures (≥ 2 km), orientated perpendicular to the small-scale structures occur at $2.5 \times v$. The direction of these large-scale structures turns as well and becomes more obvious with increasing wind speeds.

The fields of τ_{sim} are evaluated using 2D autocorrelation analysis. The results are given in Fig. 9g to Fig. 9i. Displayed are only the horizontal scales below 1 km, the 2D autocorrelation coefficients for shifts below ± 1 km. With increasing wind speeds the area covered by $P_{\tau}^2 \geq P_{\tau}^2(\xi_{\tau})$ increases. This illustrates that with increasing wind speed the size of the small-scale cloud structures increases along the predominant directions. The increased wind speed leads to stretched cloud structures along one direction. Along this predominant direction the stretching of the cloud structures smoothes their variability stronger than across this direction. This leads to more homogeneous cloud structures. The turn of the orientation of the cloud structures to the East with increasing wind speed is also represented by the fields of P_{τ}^2 .



Quantitative values for the size of the cloud inhomogeneity structures in terms of the decorrelation length ξ_τ as a function of initialization wind speed are displayed in Fig. 10a (along predominant direction) and in Fig. 10b (across predominant structure). The threshold of $P_\tau^2(\xi_\tau) = e^{-2}$ is marked by a grey dotted line. The derived values for ξ_τ^\uparrow and $\xi_\tau^{\leftrightarrow}$ are displayed in Fig. 10c as a function of the vertical mean wind speed within the cloudy region. It shows that along the predominant structure the decorrelation length ξ_τ^\uparrow increases continuously (slightly quadratic increase) with increasing wind speed. The derived decorrelation length along (ξ_τ^\uparrow) the predominant structure as a function of wind speed (vertically averaged over cloudy region) in units of m s^{-1} can be approximated by:

$$\xi_\tau^\uparrow = 31 \cdot v^2 - 31 \cdot v + 315. \quad (5)$$

Across the predominant structure (Fig. 10c) it is different, which means that for the lower wind speeds ($< 2 \times v$) no influence on P_τ^2 and ξ_τ occurs, while it is comparable (slightly quadratic increase) to the values along the predominant structures for the stronger wind speeds ($\geq 2 \times v$). The derived decorrelation length across ($\xi_\tau^{\leftrightarrow}$) the predominant structure as a function of wind speed can be approximated by:

$$\xi_\tau^{\leftrightarrow} = 60 \cdot v^2 - 183 \cdot v + 365. \quad (6)$$

Both, ξ_τ^\uparrow and $\xi_\tau^{\leftrightarrow}$ characterize the small-scale cloud inhomogeneities. Large-scale cloud structures cannot be represented due to the too small domain size. However, comparing ξ_τ^\uparrow with $\xi_\tau^{\leftrightarrow}$ shows that the directionality of the cloud structures first increases (0.5 to $2.0 \times v$) and afterwards decreases (2.0 to $3.0 \times v$) again. For the case investigated here, the threshold at $2.0 \times v$ applies to a mean v (vertically averaged over cloudy region) of 3.0 m s^{-1} .

7 Summary and Conclusions

Cloud remote sensing results (cloud optical thickness) and atmospheric profile measurements (air pressure, temperature, relative humidity, wind vector) by dropsondes from the airborne VERDI campaign conducted in April/May 2012 are exploited. The analysis focuses on a persistent cloud layer probed in close vicinity ($\leq 50 \text{ km}$) over constant surface conditions (open water; Polynia) on four consecutive days from 14 to 17 May 2012. The cloud top altitude of the cloud layer in the respective area shrunk from day to day; it decreased from about 880 m on 14 May to around 200 m on 17 May. This case was applied as a test bed for a new approach by comparing observed and simulated cloud fields.

The dropsonde profile measurements from the four consecutive days were used to initialize the cloud simulations with COSMO. It is found that COSMO captures the measured cloud altitude, cloud vertical extent, and retrieved cloud optical thickness. The comparison of the horizontal cloud inhomogeneities was performed for horizontal fields of cloud optical thickness τ using airborne observations of reflected solar radiances and from simulated 3D fields of LWC. The observed fields of cloud optical thickness τ_{meas} were aggregated to pixel sizes of 100 m. The absolute values of cloud inhomogeneity derived from COSMO are larger by a factor of two, as compared to the values obtained from the observations; the cloud inhomogeneity generated by COSMO is too low. This is mainly related to (i) the larger effective grid spacing ($\approx 3 \times 100 \text{ m}$, Skamarock et al., 2011) of



COSMO compared to the pixel size of the observations and (ii) a mismatch in timing/spacing, meaning that for the fields of τ_{sim} from COSMO the resulting 2D autocorrelation functions $P_{\tau,\text{sim}}^2$ are averaged over several time steps simulated at always the same location, while for the observed fields of τ_{meas} the resulting 2D autocorrelation functions $P_{\tau,\text{meas}}^2$ are averaged along the flight track. Furthermore, in a model intercomparison Ovchinnikov et al. (2014) revealed that COSMO underestimates the variance of the vertical wind velocity compared to other LES models and, thus, an underestimation of the standard deviation of τ_{sim} is possible. However, except for the case on 16 May the trend of the temporal evolution of the overall cloud inhomogeneity is well covered by COSMO.

Especially for the cases on 14 and 16 May the cloud structures showed a distinct directional orientation and on 15 and 17 May a still slightly directional orientation. Brümmer (1999) points out that such directed cloud structures are typical for Arctic stratus with cloud top altitudes below 1 km, which is the case here, while for Arctic stratus with cloud top altitudes larger than 1.4 km some cell structures are common. Based on a new method, proposed by Schäfer et al. (2017a), which is applied to COSMO data for the first time, 2D analysis using autocorrelation functions is used to examine directional features of the cloud structures. The investigations showed that COSMO captured the observed directional structures of the cloud inhomogeneities quite well. The wind directions of the individual cases showed a significant correlation to the direction of the predominant directional structures. During the four investigated days the orientation of the dominant directional structures within the observations turned eastwards by the same degree the wind direction changed. Similar results were found by (Houze, 1994), who stated that in case of changing wind shear cloud streets will be orientated along the mean wind direction. Here, this is reproduced for the cases with 0.5 to $2.0 \times v$.

The good agreement between the COSMO results and the observations justified a systematic sensitivity study regarding the main drivers of the cloud inhomogeneities. The wind speed was expected to be a main forcing for the degree of cloud inhomogeneity. Repeating the simulations for the case on 15 May with differently scaled initialization profiles for the wind speed, the degree of horizontal cloud inhomogeneity was significantly changed. This confirms the importance of the wind speed for cloud inhomogeneities. Furthermore, it was found that increasing wind speeds lead to larger horizontal cloud structures (increased decorrelation lengths). It was concluded that the directionality of the cloud structures first increases (0.5 to $2.0 \times v$) and afterwards decreases (2.0 to $3.0 \times v$) again. Using all averaged wind speeds (in the altitudes of the cloudy region) of the six applied wind profiles parameterizations of the decorrelation lengths along and across the strongest autocorrelation were derived, which can be used in future studies to generate cloud structures with specific sizes and shapes.

Furthermore, it was concluded that the wind direction and the atmospheric boundary layer structure are the explanation for the differences on 16 May. In contrast to the other three days a change of the wind direction of about 50° is found close to the cloud top. Moreover, the ABL is well mixed on 16 May, which increases the turbulent mixing within in the ABL and the cloud layer, and consequently influences the cloud top structure. Local differences in the wind fields at the position where the dropsonde was released and the location where the imaging spectrometer measured might be the reason that this was not equally well captured by the simulations and measurements. The difficulties of COSMO to represent the small-scale cloud structures is a further reason.

All together, cloud inhomogeneities are challenging to be captured by models and with this study a new method is applied



to combine observed and simulated fields of cloud optical thickness. Although COSMO produces more homogeneous clouds, it performed well, because it represented the directional structures and the tendency of increasing/decreasing degree of cloud inhomogeneity of most of the cases right.

8 Data availability

- 5 The fields of cloud optical thickness retrieved from the AisaEAGLE measurements are published on PANGAEA (Schäfer et al., 2017b). All other data used in this study are available upon request from the corresponding authors (michael.schaefer@uni-leipzig.de, katharina.loewe@kit.edu).

Acknowledgements. We thank Marco Paukert for introducing the COSMO setup. K. Loewe and C. Hoose acknowledge partial funding through the Helmholtz Programme "Atmosphere and Climate" and this project has received funding from the European Research Council (ERC) under the European Union's Horizon 2020 research and innovation programme under grant agreement No 714062 (ERC Starting Grant "C2Phase"). We gratefully acknowledge the support by the SFB/TR 172 "Arctic Amplification: Climate Relevant Atmospheric and SurfaCe Processes, and Feedback Mechanisms (AC)³" in Project B03 funded by the DFG. We thank Eike Bierwirth for organizing and performing the imaging spectrometer measurements during the VERDI campaign. Furthermore, we thank Paul Vochezer, Martin Schnaiter and Emma Järvinen for providing the SID3 data. We are grateful to the Alfred Wegener Institute, Helmholtz Centre for Polar and Marine Research, Bremerhaven, Germany for supporting the VERDI campaign with the aircraft and manpower. In addition we like to thank Kenn Borek Air Ltd., Calgary, Canada for the great pilots who made the complicated measurements possible. For excellent ground support with offices and accommodations during the campaign we are grateful to the Aurora Research Institute, Inuvik, Canada.

10
15



References

- Barrett, A. I., Hogan, R. J. and Forbes, R. M.: Why are mixed-phase altocumulus clouds poorly predicted by large-scale models? Part 1. Physical processes, *J. Geophys. Res. Atmos.*, 122, <https://doi.org/10.1002/2016JD026321>, 2017.
- Barrett, A. I., Hogan, R. J. and Forbes, R. M.: Why are mixed-phase altocumulus clouds poorly predicted by large-scale models? Part 2. Vertical resolution sensitivity and parameterization, *J. Geophys. Res. Atmos.*, 122, <https://doi.org/10.1002/2016JD026322>, 2017.
- 5 Bierwirth, E., Ehrlich, A., Wendisch, M., Gayet, J.-F., Gourbeyre, C., Dupuy, R., Herber, A., Neuber, R., and Lampert, A.: Optical thickness and effective radius of Arctic boundary-layer clouds retrieved from airborne nadir and imaging spectrometry, *Atmos. Meas. Tech.*, 6, 1189–1200, <https://doi.org/10.5194/amt-6-1189-2013>, 2013.
- Brümmer, B.: Roll and Cell Convection in Wintertime Arctic Cold-Air Outbreaks, *J. Atmos. Sci.*, 56, 2613–2636, [https://doi.org/10.1175/1520-0469\(1999\)056<2613:RACCIW>2.0.CO;2](https://doi.org/10.1175/1520-0469(1999)056<2613:RACCIW>2.0.CO;2), 1999.
- 10 Cahalan, R.: Bounded cascade clouds: albedo and effective thickness, *Nonlin. Proc. Geophys.*, 1, 1994.
- Chylek, P. and Borel, C.: Mixed phase cloud water/ice structure from satellite data high spatial resolution, *Geophys. Res. Lett.*, 31, L14104, <https://doi.org/10.1029/2004GL020428>, 2004.
- Coleman, D. M.: Evaluation of the Performance of the Dropsonde Humidity Sensor in Clouds, SOARS, 2003.
- 15 Costa, A., Meyer, J., Afchine, A., Luebke, A., Günther, G., Dorsey, J. R., Gallagher, M. W., Ehrlich, A., Wendisch, M., Baumgardner, D., Wex, H., and Krämer, M.: Classification of Arctic, midlatitude and tropical clouds in the mixed-phase temperature regime, *Atmos. Chem. Phys.*, 17, 12219–12238, <https://doi.org/10.5194/acp-17-12219-2017>, 2017.
- Curry, J. A., Rossow, W. B., Randall, D., and Schramm, J. L.: Overview of Arctic cloud and radiation characteristics, *J. Climate*, 9, 1.731–1.764, [https://doi.org/10.1175/1520-0442\(1996\)009<1731:OOACAR>2.0.CO;2](https://doi.org/10.1175/1520-0442(1996)009<1731:OOACAR>2.0.CO;2), 1996.
- 20 Davis, A., Marshak, A., Gerber, H., and Wiscombe, W.: Horizontal structure of marine boundary layer clouds from centimeter to kilometer scales, *J. Geophys. Res.*, 104, 6123–6144, 1999b.
- Dee, D. P., Uppala, S. M., Simmons, A. J., Berrisford, P., Poli, P., Kobayashi, S., Andrae, U., Balmaseda, M. A., Balsamo, G., Bauer, P., Bechtold, P., Beljaars, A. C. M., van de Berg, L., Bidlot, J., Bormann, N., Delsol, C., Dragani, R., Fuentes, M., Geer, A. J., Haimberger, L., Healy, S. B., Hersbach, H., Hólm, E. V., Isaksen, I., Kållberg, P., Köhler, M., Matricardi, M., McNally, A. P., Monge-Sanz, B.
- 25 M., Morcrette, J.-J., Park, B.-K., Peubey, C., de Rosnay, P., Tavolato, C., Thépaut, J.-N. and Vitart, F.: The ERA-Interim reanalysis: configuration and performance of the data assimilation system, *Q.J.R. Meteorol. Soc.*, 137, 553–597, <https://doi.org/10.1002/qj.828>, 2011.
- Ehrlich, A., Bierwirth, E., Iстомnia, L., and Wendisch, M.: Combined retrieval of Arctic liquid water cloud and surface snow properties using airborne spectral solar remote sensing, *Atmos. Chem. Tech.*, 10, 3215–3230, <https://doi.org/10.5194/amt-10-3215-2017>, 2017.
- Field, P.R., Hogan, R.J., Brown, P.R.A., Illingworth, A.J., Choullarton, T.W., Kaye, P.H., Hirst, E., Greenaway, R.: Simultaneous radar and aircraft observations of mixed-phase cloud at the 100 m scale, *Q. J. R. Meteorol. Soc.*, 130, 1877–1904, <https://doi.org/10.1256/qj.03.102>, 2004.
- 30 Hinkelmann, L. M.: Differences between along-wind and cross-wind solar irradiance variability on small spatial scales, *Sol. Energy*, 88, 192–203, <https://doi.org/10.1016/j.solener.2012.11.011>, 2013.
- Hock, T. F. and Franklin, J. L.: The NCAR GPS dropwindsonde, *Bull. Amer. Meteorol. Soc.*, 80, 407–420, [https://doi.org/10.1175/1520-0477\(1999\)080<0407:TNGD>2.0.CO;2](https://doi.org/10.1175/1520-0477(1999)080<0407:TNGD>2.0.CO;2), 1999.
- Robert A. Houze, Jr.: *Cloud Dynamics*, International Geophysics series, 53, p. 166, 1994.



- Intrieri, J. M., Shupe, M. D., Uttal, T., and McCarty, B. J.: An annual cycle of Arctic cloud characteristics observed by radar and lidar at SHEBA, *J. Geophys. Res.*, 107, (C10), <https://doi.org/10.1029/2000JC000423>, 2002.
- Iwabuchi, H. and Hayasaka, T.: Effects of cloud horizontal inhomogeneity on the optical thickness retrieved from moderate-resolution satellite data, *J. Atmos. Sci.*, 59, 2227–2242, [https://doi.org/10.1175/1520-0469\(2002\)059<2227:EOCHIO>2.0.CO;2](https://doi.org/10.1175/1520-0469(2002)059<2227:EOCHIO>2.0.CO;2), 2002.
- 5 Jacobson, L., Vihma, T., Jakobson, E., Palo, T., Männik, A., and Jaagus, J.: Low-level jet characteristics over the Arctic Ocean in spring and summer, *Atmos. Chem. Phys.*, 13, 11089–11099, <https://doi.org/10.5194/acp-13-11089-2013>, 2013.
- Klein, S. A., McCoy, R. B., Morrison, H., Ackerman, A. S., Avramov, A., de Boer, G., Chen, M., Cole, J. N. S., Del Genio, A. D., Falk, M., Foster, M. J., Fridlind, A., Golaz, J.-C., Hashino, T., Harrington, J. Y., Hoose, C., Khairoutdinov, M. F., Larson, V. E., Liu, X., Luo, Y., McFarquhar, G. M., Menon, S., Neggers, R. A. J., Park, S., Poellot, M. R., Schmidt, J. M., Sednev, I., Shipway, B. J., Shupe, M. D.,
10 Spangenberg, D. A., Sud, Y. C., Turner, D. D., Veron, D. E., Salzen, K. v., Walker, G. K., Wang, Z., Wolf, A. B., Xie, S., Xu, K.-M., Yang, F., and Zhang, G.: Intercomparison of model simulations of mixed-phase clouds observed during the ARM Mixed-Phase Arctic Cloud Experiment. I: single-layer cloud, *Q. J. R. Meteorol. Soc.*, 135, 979–1002, <https://doi.org/10.1002/qj.416>, 2009.
- Klingebiel, M.; de Lozar, A.; Molleker, S.; Weigel, R.; Roth, A.; Schmidt, L.; Meyer, J.; Ehrlich, A.; Neuber, R.; Wendisch, M. and Borrmann, S.: Arctic low-level boundary layer clouds: in situ measurements and simulations of mono- and bimodal supercooled droplet size
15 distributions at the top layer of liquid phase clouds, *Atmos. Chem. Phys.*, 15, 617–631, <https://doi.org/10.5194/acp-15-617-2015>, 2015.
- Kopec, M. K., Malinowskia, S. P. and Piotrowski, Z. P.: Effects of wind shear and radiative cooling on the stratocumulus-topped boundary layer, *Q. J. R. Meteorol. Soc.* 142: 3222–3233, <https://doi.org/10.1002/qj.2903>, 2016.
- Korolev, A.: Limitations of the Wegener–Bergeron–Findeisen Mechanism in the Evolution of Mixed-Phase Clouds, *J. Atmos. Sci.*, 64, 3372–3375, <https://doi.org/10.1175/JAS4035.1>, 2007.
- 20 Lawson, R.P., Stamnes, K., Stamnes, J., Zmarzly, P., Koskuliks, J., Roden, C., Mo, Q., Carrithers, M., and Bland, G.L.: Deployment of a Tethered-Balloon System for Microphysics and Radiative Measurements in Mixed-Phase Clouds at Ny-Ålesund and South Pole, *J. Atmos. Ocean. Tech.*, 28, 656–670, <https://doi.org/10.1175/2010JTECHA1439.1>, 2010.
- Lindsay, R., Wensnahan, M., Schweiger, A., and Zhang, J.: Evaluation of seven different atmospheric reanalysis products in the arctic, *J. Climate*, 27, 2588–2605, <https://doi.org/10.1175/JCLI-D-13-00014.1>, 2014.
- 25 Loewe, K., Ekman, A. M. L., Paukert, M., Sedlar, J., Tjernström, M., and Hoose, C.: Modelling micro- and macrophysical contributors to the dissipation of an Arctic mixed-phase cloud during the Arctic Summer Cloud Ocean Study (ASCOS), *Atmos. Chem. Phys.*, 17, 6693–6704, <https://doi.org/10.5194/acp-17-6693-2017>, 2017.
- Marchand, R. T., Ackermann, T.P., and Moroney, C.: An assessment of Multiangle Imaging Spectroradiometer (MISR) stereo-derived cloud top heights and cloud top winds using ground-based radar, lidar, and microwave radiometers, *J. Geophys. Res.*, 112, D06204,
30 <https://doi.org/10.1029/2006JD007091>, 2007.
- Marshak, A., Davis, A., Wiscombe, W., and Cahalan, R.: Radiative smoothing in fractal clouds, *J. Geophys. Res.*, 100, 26 247–26 261, 1995.
- McFarquhar, G.M., Zhang, G., Poellot, M.R., Kok, G.L., McCoy, R., Tooman, T., Fridlind, A., and Heymsfield, A.J.: Ice properties of single-layer stratocumulus during the Mixed-Phase Arctic Cloud Experiment: 1. Observations, *J. Geophys. Res.*, 112, D24201, <https://doi.org/10.1029/2007JD008633>, 2007.
- 35 McFarquhar, G.M., S. Ghan, J. Verlinde, A. Korolev, J.W. Strapp, B. Schmid, J.M. Tomlinson, M. Wolde, S.D. Brooks, D. Cziczo, M.K. Dubey, J. Fan, C. Flynn, I. Gultepe, J. Hubbe, M.K. Gilles, A. Laskin, P. Lawson, W.R. Leitch, P. Liu, X. Liu, D. Lubin, C. Mazzoleni, A. Macdonald, R.C. Moffet, H. Morrison, M. Ovchinnikov, M.D. Shupe, D.D. Turner, S. Xie, A. Zelenyuk, K. Bae, M. Freer, and A. Glen: Indirect and Semi-direct Aerosol Campaign., *Bull. Amer. Meteor. Soc.*, 92, 183–201, <https://doi.org/10.1175/2010BAMS2935.1>, 2011.



- Mellado, J. P.: Cloud-Top Entrainment in Stratocumulus Clouds, *Ann. Rev. of Fluid Mech.*, 49, 145–69, <https://doi.org/10.1146/annurev-fluid-010816-060231>, 2017.
- Mioche, G., Jourdan, O., Ceccaldi, M., and Delanoë, J.: Variability of mixed-phase clouds in the Arctic with a focus on the Svalbard region: a study based on spaceborne active remote sensing, *Atmos. Chem. Phys.*, 15, 2445–2461, <https://doi.org/10.5194/acp-15-2445-2015>, 5 2015.
- Morrison, H., de Boer, G., Feingold, G., Harrington, J., Shupe, M. D. and Sulia, K.: Resilience of persistent Arctic mixed-phase clouds, *Nat. Geosci.*, 5, 11–17, <https://doi.org/10.1038/NGEO1332>, 2012.
- Oreopoulos, L., Cahalan, R., Marshak, A., and Wen, G.: A new normalized difference cloud retrieval technique applied to Landsat radiances over the Oklahoma ARM site, *J. Appl. Meteorol.*, 39, 2305–2321, 2000.
- 10 Oreopoulos, L. and Cahalan, R. F.: Cloud Inhomogeneity from MODIS, *J. Climate*, 18, 5110–5124, 2005.
- Ovchinnikov, M., Ackerman, A. S., Avramov, A., Cheng, A., Fan, J., Fridlind, A. M., Ghan, S., Harrington, J., Hoose, C., Korolev, A., McFarquhar, G. M., Morrison, H., Paukert, M., Savre, J., Shipway, B. J., Shupe, M. D., Solomon, A., and Sulia, K.: Intercomparison of large-eddy simulations of Arctic mixed-phase clouds: Importance of ice size distribution assumptions, *J. Adv. Model. Earth Syst.*, 6, 223–248, <https://doi.org/10.1002/2013MS000282>, 2014.
- 15 Paukert, M. and Hoose, C.: Modeling immersion freezing with aerosol-dependent prognostic ice nuclei in Arctic mixed-phase clouds, *J. Geophys. Res. Atmos.*, 14, 9073–9092, <https://doi.org/10.1002/2014JD021917>, 2014.
- Pedersen, J. G., Malinowski, S. P. and Grabowski, W. W.: Resolution and domain-size sensitivity in implicit large-eddy simulation of the stratocumulus-topped boundary layer, *J. Adv. Model. Earth Syst.*, 8, 885–903, <https://doi.org/10.1002/2015MS000572>, 2016.
- Rossow, W. B., and Schiffer, R. A.: ISCCP cloud data products, *Bull. Amer. Meteor. Soc.*, 72, 2–20, 1991.
- 20 Schäfer, M., Bierwirth, E., Ehrlich, A., Heyner, F., and Wendisch, M.: Retrieval of cirrus optical thickness and assessment of ice crystal shape from ground-based imaging spectrometry, *Atmos. Meas. Tech.*, 6, 1855–1868, <https://doi.org/10.5194/amt-6-1855-2013>, 2013.
- Schäfer, M., Bierwirth, E., Ehrlich, A., Jäkel, E., and Wendisch, M.: Airborne observations and simulations of three-dimensional radiative interactions between Arctic boundary layer clouds and ice floes, *Atmos. Chem. Phys.*, 15, 8147–8163, <https://doi.org/10.5194/acp-15-8147-2015>, 2015.
- 25 Schäfer, M., Bierwirth, E., Ehrlich, A., Jäkel, E., Werner, F., and Wendisch, M.: Directional, horizontal inhomogeneities of cloud optical thickness fields retrieved from ground-based and airborne spectral imaging, *Atmos. Chem. Phys.*, 17, 2359–2372, <https://doi.org/10.5194/acp-17-2359-2017>, 2017.
- Schäfer, M., Bierwirth, E., Ehrlich, A., Jäkel, E., Werner, F., and Wendisch, M.: Cloud optical thickness retrieved from horizontal fields of reflected solar spectral radiance measured with AisaEAGLE during VERDI campaign 2012, PANGAEA, 30 <https://doi.org/10.1594/PANGAEA.874798>, 2017.
- Schättler, U., Doms, G., and Schraff, C.: A description of the non-hydrostatic regional COSMO-model, part VII: user's guide, <http://www.cosmo-model.org>, 2015.
- Schröder, M.: Multiple scattering and absorption of solar radiation in the presence of three-dimensional cloud fields, Ph.D. thesis, Fachbereich Geowissenschaften der Freien Universität Berlin, 2004.
- 35 Serreze, M. C., and Barry, R. G.: Processes and impacts of Arctic amplification: A research synthesis, *Global Planet. Change*, 77, 85–96, <https://doi.org/10.1016/j.gloplacha.2011.03.004>, 2011.
- Shiobara, M., Masanori, Y., and Kobayashi, H.: A polar cloud analysis based on Micro-pulse Lidar measurements at Ny-Alesund, Svalbard and Syowa, Antarctica, *Phys. Chem. Earth*, 28, 1205–1212, <https://doi.org/10.1016/j.pce.2003.08.057>, 2003.



- Shupe, M. D. and Intrieri, J. M.: Cloud radiative forcing of the Arctic surface: The influence of cloud properties, surface albedo, and solar zenith angle, *J. Climate*, 17, 616–628, 2004.
- Shupe, M. D., Matrosov, S. Y., and Uttal, T.: Mixed-Phase Cloud Properties Derived from Surface-Based Sensors at SHEBA, *J. Atmos. Sci.*, 63, 697–711, <https://doi.org/10.1175/JAS3659.1>, 2006.
- 5 Shupe, M. D., Kollias, P., Persson, P.O.G., and McFarquhar, G.M.: Vertical Motions in Arctic Mixed-Phase Stratiform Clouds, *J. Atmos. Sci.*, 65, 1304–1321, <https://doi.org/10.1175/2007JAS2479.1>, 2008.
- Shupe, M. D., Walden, V. P., Eloranta, E., Uttal, T., Campbell, J. R., Starkweather, S. M., and Shiobara, M.: Clouds at Arctic Atmospheric Observatories. Part I: Occurrence and Macrophysical Properties, *J. Appl. Meteorol. Clim.*, 50, 626–644, <https://doi.org/10.1175/2010JAMC2467.1>, 2011.
- 10 Skamarock, W. C.: Evaluating Mesoscale NWP Models Using Kinetic Energy Spectra, *Mon. Wea. Rev.*, 132, 3019–3032, <https://doi.org/10.1175/MWR2830.1>, 2004.
- Stevens, R. G., Loewe, K., Dearden, C., Dimitrelos, A., Possner, A., Eirund, G. K., Raatikainen, T., Hill, A. A., Shipway, B. J., Wilkinson, J., Romakkaniemi, S., Tonttila, J., Laaksonen, A., Korhonen, H., Connolly, P., Lohmann, U., Hoose, C., Ekman, A. M. L., Carslaw, K. S. and Field, P. R.: A Model Intercomparison of CCN-Limited Tenuous Clouds in the High Arctic, *Atmos. Chem. Phys. Discuss.*, <https://doi.org/10.5194/acp-2017-1128>, in review, 2017.
- 15 Szczap, F., Isaka, H., Saute, M., and Guillemet, B.: Effective radiative properties of bounded cascade nonabsorbing clouds: Definition of the equivalent homogeneous cloud approximation, *J. Geophys. Res.*, 105, 20 617–20 633, 2000.
- Varnai, T. and Marshak, A.: Observations of Three-Dimensional Radiative Effects that Influence MODIS Cloud Optical Thickness Retrievals, *J. Atmos. Sci.*, 59, 1607–1618, 2001.
- 20 Vochezer, P., Järvinen, E., Wagner, R., Kupiszewski, P., Leisner, T., and Schnaiter, M.: In situ characterization of mixed phase clouds using the Small Ice Detector and the Particle Phase Discriminator, *Atmos. Meas. Tech.*, 9, 159–177, <https://doi.org/10.5194/amt-9-159-2016>, 2016.
- Vavrus, S.: The Impact of Cloud Feedbacks on Arctic Climate under Greenhouse Forcing, *J. Climate*, 17, 603–615, [https://doi.org/10.1175/1520-0442\(2004\)017<0603:TIOCFO>2.0.CO;2](https://doi.org/10.1175/1520-0442(2004)017<0603:TIOCFO>2.0.CO;2), 2004.
- 25 Wendisch, M., Yang, P., and Ehrlich, A., (Eds.): Amplified climate changes in the Arctic: Role of clouds and atmospheric radiation, 132, 1–34, *Sitzungsberichte der Sächsischen Akademie der Wissenschaften zu Leipzig, Mathematisch-Naturwissenschaftliche Klasse*, S. Hirzel Verlag, Stuttgart/Leipzig, 2013.
- Wendisch, M., Brückner, M., Burrows, J. P., Crewell, S., Dethloff, K., Ebell, K., Lüpkes, Ch., Macke, A., Notholt, J., Quaas, J., Rinke, A., and Tegen, I.: Understanding causes and effects of rapid warming in the Arctic, *EOS*, 98(8), 22–26, <https://doi.org/10.1029/2017EO064803>,
30 2017.